

# Nanoscale

Accepted Manuscript



This is an *Accepted Manuscript*, which has been through the Royal Society of Chemistry peer review process and has been accepted for publication.

*Accepted Manuscripts* are published online shortly after acceptance, before technical editing, formatting and proof reading. Using this free service, authors can make their results available to the community, in citable form, before we publish the edited article. We will replace this *Accepted Manuscript* with the edited and formatted *Advance Article* as soon as it is available.

You can find more information about *Accepted Manuscripts* in the [Information for Authors](#).

Please note that technical editing may introduce minor changes to the text and/or graphics, which may alter content. The journal's standard [Terms & Conditions](#) and the [Ethical guidelines](#) still apply. In no event shall the Royal Society of Chemistry be held responsible for any errors or omissions in this *Accepted Manuscript* or any consequences arising from the use of any information it contains.



Journal Name

ARTICLE

## Highly Efficient Electrocatalyst for Oxygen Reduction Reaction: Phosphorus and Nitrogen Co-Doped Hierarchically Ordered Porous Carbon Derived from Iron-Functionalized Polymer

Received 00th January 20xx,  
Accepted 00th January 20xx

DOI: 10.1039/x0xx00000x

www.rsc.org/

Chengwei Deng,<sup>a,b</sup> Hexiang Zhong,<sup>a,\*</sup> Xianfeng Li,<sup>a,c</sup> Lan Yao,<sup>a,b</sup> and Huamin Zhang<sup>a,c,\*</sup>

Heteroatom-doped carbon materials have shown respectable activity for the oxygen reduction reaction (ORR) in alkaline media. However, the performance of these materials is not satisfactory for energy conversion devices, such as fuel cells. Here, we demonstrate a new type of phosphorus and nitrogen co-doped hierarchically ordered porous carbon (PNHOPC) derived from an iron-functionalized mesoporous polymer through an evaporation-induced self-assembly process that simultaneously combines the carbonization and nitrogen doping processes. The soft template and the nitrogen doping process facilitate the formation of the hierarchically ordered structure for the PNHOPC. The catalyst possesses a large surface area ( $1118 \text{ cm}^2 \text{ g}^{-1}$ ) and a pore volume of  $1.14 \text{ cm}^3 \text{ g}^{-1}$ . Notably, it exhibits excellent ORR catalytic performance, superior stability and methanol tolerance in acidic electrolytes, thus making the catalyst promising for fuel cells. The correlations between the unique pore structure and the nitrogen and phosphorus configuration of the catalysts with the high catalytic activity are thoroughly investigated.

### 1. Introduction

Intensive research efforts have recently been devoted to the development of efficient, cost-effective and durable alternative catalysts for the oxygen reduction reaction (ORR).<sup>1–3</sup> Platinum-based electrocatalysts are widely used for the ORR. However, Pt is expensive and scarce, which hinders the widespread commercialization of fuel cells and metal–air batteries. Although non-noble catalysts have potential for use as ORR catalysts, they still suffer from insufficient activity and/or low stability compared to Pt-based catalysts, particularly in acidic media.<sup>4</sup>

Recently, heteroatom-doped carbon-based materials with abundant free-flowing  $\pi$  electrons,<sup>5</sup> high electrical conductivity and corrosion resistance have been exploited as the most promising non-precious metal catalysts.<sup>6, 7</sup> It has been reported that heteroatom dopants (e.g., nitrogen, phosphorous, and boron) can greatly enhance the ORR activity and impart the carbon material with an improved electronic structure, defect sites and optimal surface properties.<sup>8</sup> For

example, in N-doped carbon materials, the lone-pair electron from nitrogen activates the carbon  $\pi$  electrons, leading to charge delocalization of the carbon atoms, which is favorable for the adsorption of  $\text{O}_2$ . Phosphorus has smaller electron negativity (2.19) and a larger atomic radius than carbon. And it has the same number of valence electrons as nitrogen and often shows similar chemical properties, which make it an astute choice as a dopant to carbon materials and thus is expected to enhance the catalytic activity as well.<sup>9</sup> P-doped carbon catalysts show promising activity toward the ORR, in which the ORR pathway on these P-containing carbons is a two-electron pathway that evidently produces  $\text{H}_2\text{O}$ .<sup>10, 11</sup> Additionally, doping carbon materials with transition metal ions can efficiently improve the ORR catalytic activity.<sup>7, 12, 13</sup> Fe and Co are considered as the most efficient additives for doping carbon materials, primarily due to the coordination of the metal cations with C-N functionalities and their ability to form active sites.<sup>14–17</sup>

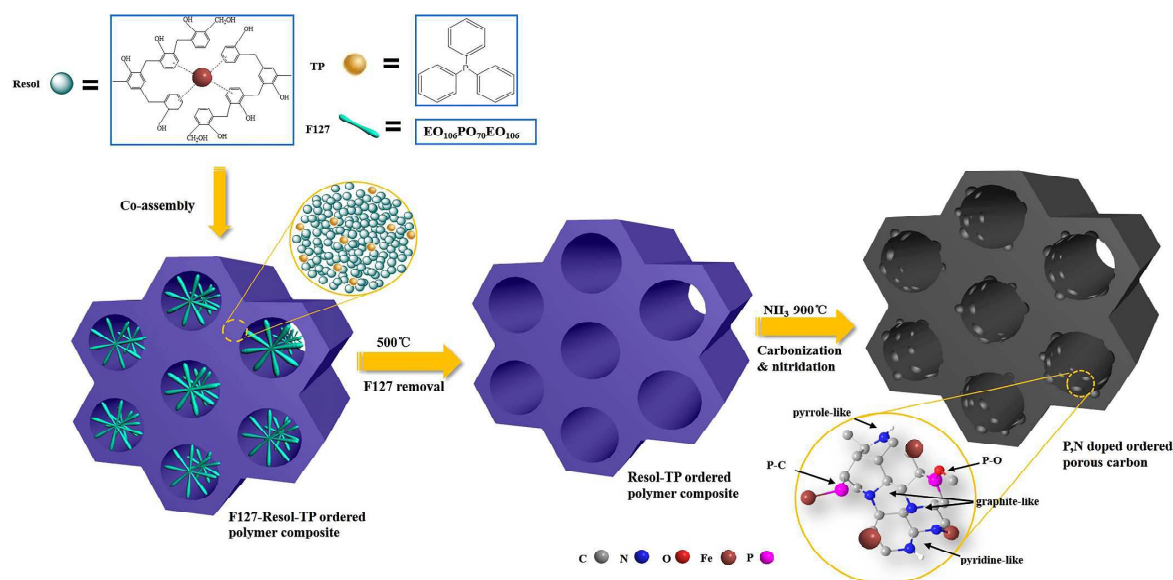
Ordered mesoporous carbon (OMC), which possesses a high specific surface area, electrical conductivity and optimal mass transport characteristics, has been widely used in  $\text{CO}_2$  capture, super capacitors and fuel cells.<sup>18–20</sup> More importantly, OMC provides a simple but effective way to control the pore structure and pore size distribution. Doping OMC with heteroatoms and transition metal ions in appropriate proportions, namely, combining the advantage of the tunable structure and the positive role of dopants, can produce a type of highly promising non-precious metal ORR catalyst.<sup>6, 20, 21</sup>

*a* Division of Energy Storage, Dalian National Laboratory for Clean Energy (DNL)  
Dalian Institute of Chemical Physics, Chinese Academy of Sciences  
Dalian 116023, China

*b* Graduate University of the Chinese Academy of Sciences  
Beijing 100049, China

*c* Collaborative Innovation Centre of Chemistry for Energy Materials (iChem),  
Dalian 116023 (P.R. China)

Corresponding authors:  
zhanghm@dicp.ac.cn; zhonghexiang@dicp.ac.cn



**Scheme 1.** Illustration of the synthesis and heteroatom doping process for PNHOPC

In this article, we describe the development of a phosphorus and nitrogen co-doped ordered porous carbon derived from an iron-functionalized mesoporous polymer. The ordered mesostructured polymers are prepared from phenol formaldehyde resin (RF) as carbon precursors and are simultaneously functionalized by the iron precursor via the soft-template strategy. The N-doped hierarchically ordered porous carbon (NHOPC) is subsequently synthesized through carbonization of the resulting mesostructured organic material in  $\text{NH}_3$ . The doping of P into the N-doped hierarchically ordered porous carbon (PNHOPC) is performed through the addition of triphenylphosphine during the synthesis of the RF polymers. The resulting PNHOPC possesses a controllable nitrogen and phosphorus content, a high surface area, and hierarchically interconnected porous structures. Remarkably, the PNHOPC catalyst exhibits superior ORR activity in acidic media, achieving approximately 51% mass activity of the commercial JM-20% Pt/C catalyst. It also presents higher catalytic activity than N-doped carbon and P-doped carbon synthesized using a similar method. Moreover, the developed catalyst also possesses high stability and excellent methanol tolerance.

## 2. Experimental Section

### 2.1 Catalyst preparation

#### 2.1.1 Preparation of iron functionalized resol precursor

Iron-functionalized resol, a soluble phenolic resin, and Pluronic F127 (Mw=12600, PEO106-PPO70-PEO106, Aldrich) were used as the carbon source and the soft template, respectively. First, 2 g of phenol (P) was dispersed in water at 50 °C in a beaker and mixed with 0.43 g of a 20 wt. % sodium hydroxide (NaOH) aqueous solution. Then, 3.2 ml of a formaldehyde (F) solution (37 wt. %) was added dropwise, followed by stirring for 1-2 hours at 75 °C to form the phenolic resin solution. The pH of

the aforementioned solution was adjusted to  $\sim 7.0$  with a 0.5 M HCl solution, and the water was removed by vacuum evaporation at 60 °C to obtain the phenolic resins. Iron-functionalized phenolic resol was obtained after mixing the resins that was dissolved in 20 ml of ethanol with  $\text{FeSO}_4 \cdot 7\text{H}_2\text{O}$  (0.3 g, Tianjin Damao Chemical Co. Ltd) at 40 °C.

#### 2.1.2 Preparation of PNHOPC

The PNHOPC was prepared via the soft template method after pyrolysis of the resulting ordered mesostructured polymer in ammonia (Scheme 1). After stirring for 30 minutes, 5 ml of the iron-functionalized resol precursor was added to a F127/ethanol mixture. Then, 0.17 g of Triphenylphosphine (0.17 g, Sinopharm Chemical Reagent Co. Ltd.) was added as the phosphine precursor. When the mixture turned dark purple, the solution was poured into a large watch glass, and ethanol was evaporated at room temperature for 12 hours, followed by heating in an oven at 120 °C for 12 hours. Subsequently, the products were scraped under the watch glass. The resulting polymer was pyrolyzed under an ammonia atmosphere with a gas flow rate of 60 ml  $\text{min}^{-1}$  in a tube furnace. The temperature was increased to 500 °C at a heating rate of 2 °C/min, and then it was increased to 900 °C at a rate of 1 °C/min. Carbonization was performed at 900 °C for one hour. The PNHOPC was obtained after grinding.

#### 2.1.3 Preparation of NHOPC

The precursor solution was the same as that for the synthesis of PNHOPC. During the synthesis, 5 ml of the resol precursor resol was added to 20 g of a F127 ethanol solution (4 wt. %), and then the mixture was stirred for 30 min. After a homogeneous solution was obtained, the calcination was carried out using the same procedure as PNHOPC. After grinding, NHOPC was obtained.

#### 2.1.4 Preparation of PHOPC

The precursor solution was the same as that for the synthesis of PNHOPC. During the synthesis, 5 ml of the resol precursor

resol was added to 20 g of a F127 ethanol solution (4 wt. %), and the mixture was stirred for 30 min. Then, 0.17 g of Triphenylphosphine (0.17 g, Sinopharm Chemical Reagent Co. Ltd.) was added as the phosphine precursor. After a homogeneous solution was obtained, the resulting polymer was pyrolyzed under argon atmosphere with a gas flow rate of 60 ml min<sup>-1</sup> in a tube furnace. The calcination was carried out using the same procedure as PNHOPC. After grinding, PHOPC was obtained.

Commercial Pt/C (20 wt. %) catalysts were purchased from the Johnson Matthey company as comparison.

## 2.2 Physical characterizations

The crystal structures of the prepared samples were characterized using powder X-ray diffraction (XRD). The XRD measurements were performed on a Rigaku D/max 2400 X-ray diffractometer using graphite-monochromated Cu K $\alpha$  radiation ( $\lambda=0.1541$  nm). A scan rate of 0.02  $^{\circ}$  s<sup>-1</sup> was applied to record diffraction patterns in the 2 $\theta$  ranges from 0.5  $^{\circ}$  to 5  $^{\circ}$  (low-angle) and from 10  $^{\circ}$  to 80  $^{\circ}$  (wide-angle). Nitrogen sorption isotherms were measured at 77 K using a Micromeritics ASAP 2020 surface area and porosity analyzer. Prior to the measurements, the samples were degassed under vacuum at 300  $^{\circ}$ C for 4 h. The Brunauer-Emmett-Teller (BET) method was utilized to calculate the specific surface areas. Using the Barrett-Joyner-Halenda (BJH) model, the pore volumes and pore size distributions were derived from the adsorption branches of the isotherms at a relative pressure P/P<sub>0</sub> of 0.974. Transmission electron microscopy (TEM) experiments were conducted using a JEOL JEM-2000EX (120 kV) microscope. The samples were dispersed in ethanol and added dropwise onto the grid before characterization. XPS experiments were performed on a VG ESCALAB250 spectrometer using Al K $\alpha$  radiation and operating at a power of 300 W. The XPS binding energies were calibrated by referencing to adventitious carbon (C1s =284.6 eV), and the other peak positions were calibrated according to the C1s peak.

## 2.3 Electrochemical measurements

The electrochemical properties were examined using a three-electrode beaker cell equipped with a Pt sheet counter

electrode (Tianjin Aidahengsheng Technology Co., LTD, Pt253), a saturated calomel reference electrode (Shanghai Leici Co., 212), and a rotating ring disk electrode (Tianjin Aidahengsheng Technology Co., LTD, GC120) using an electrochemical analyzer (CH Instruments, Inc., Model 660B) and a rotator (PINE Instrument Co.). The working electrodes were prepared using the thin-film electrode method, as described in our previous work. The detailed procedure is as follows: 5 mg of catalyst and 50  $\mu$ l of a 5 wt. % Nafion<sup>®</sup> solution were dispersed in 1 ml of isopropanol, followed by ultrasonic treatment for 30 min to form a homogeneous slurry. Then, 10  $\mu$ l of the slurry was dropped onto the glassy carbon of a rotating ring disk electrode (0.1256 cm<sup>2</sup>) with a catalyst loading of 0.38 mg cm<sup>-2</sup>. All potentials were converted and referenced to the standard hydrogen electrode (SHE). Ten cycles of cyclic voltammetry (CV) experiments were conducted in a deaerated 0.5 M H<sub>2</sub>SO<sub>4</sub> electrolyte for activation of the catalysts with a scan rate of 50 mV/s from -0.25 to 0.96 V (vs. SCE). The ORR experiments were conducted in an O<sub>2</sub>-saturated 0.5 M H<sub>2</sub>SO<sub>4</sub> electrolyte using a scan rate of 5 mV/s and a rotating velocity of 1600 rpm from 0.90 to -0.20 V (vs. SCE). For comparison of the ORR activity, commercially obtained Pt/C (20 wt. %, JM Co.) was also examined under the same conditions. The methanol tolerance was examined through current-time chronoamperometry measurements performed at 0.46 V (vs. SCE) in 0.5 M H<sub>2</sub>SO<sub>4</sub> with continuous oxygen bubbling. Durability was measured by obtaining the ORR performance before and after 2000 cycles of CV in 0.5 M H<sub>2</sub>SO<sub>4</sub> with a scan rate of 100 mV/s from -0.25 to 0.96 V (vs. SCE). The first-order Koutecky-Levich (K-L) equation<sup>22</sup> was used to analyze the RDE data of the ORR at different rotation rates to determine the number of electrons (n) consumed per O<sub>2</sub> molecule.

$$-\frac{1}{J} = -\frac{1}{J_k} + \frac{1}{0.62nFD^{2/3}\nu^{-1/6}C_0\omega^{1/2}} \quad (1)$$

$$B = 0.62nFD^{2/3}\nu^{-1/6}C_0 \quad (2)$$

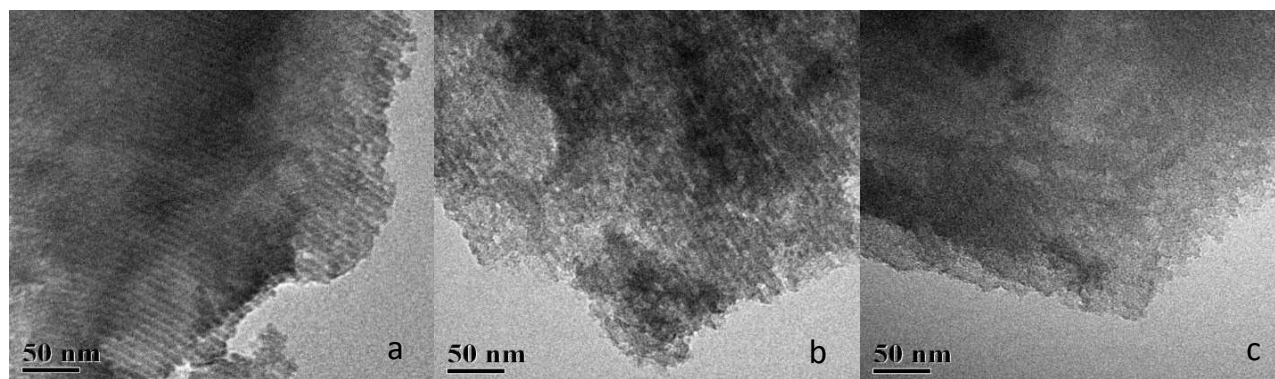


Figure 1. TEM images of (a) PHOPC, (b) NHOPC, and (c) PNHOPC.

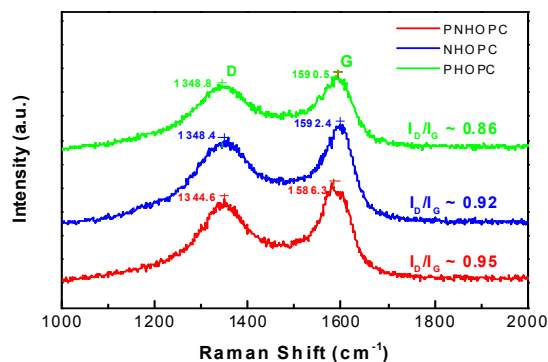


Figure 2. Raman spectra results of the prepared catalysts and the calculated  $I_D/I_G$  values.

where  $J$  is the measured current density,  $J_k$  is the kinetic current density,  $\omega$  is the rotation rate ( $\text{rad s}^{-1}$ ),  $n$  is the electron transfer number,  $F$  is the Faraday constant ( $96,485 \text{ C mol}^{-1}$ ), and  $D$  and  $C_0$  are the diffusion co-efficiency of dissolved oxygen in  $0.5 \text{ M H}_2\text{SO}_4$  ( $1.9 \times 10^{-5} \text{ cm}^2 \text{ s}^{-1}$ ) and the bulk concentration of dissolved oxygen in the electrolyte ( $0.843 \times 10^{-6} \text{ mol L}^{-1}$ ), respectively.  $\nu$  is the kinematic viscosity of the electrolyte ( $0.01128 \text{ cm}^2 \text{ s}^{-1}$ ).

## 3. Results and Discussion

### 3.1 Characterizations

The morphology and pore structure of the synthesized PHOPC, NHOPC and PNHOPC were investigated with TEM images viewed from the  $[1\ 1\ 0]$  direction (Figure 1). The typical stripe-like and hexagonally arranged structure can be observed on the PHOPC, which indicate ordered mesostructure and highly uniform pore distribution.<sup>23</sup> For the NHOPC, ordered parallel channels can also be visualized, although the regularity is not as good as that of the PHOPC especially at the edge of the carbon, suggesting a strong etching effect of the N-doping process. The unit cell parameters of PHOPC and NHOPC estimated from the TEM images are 8.1 and 9.1 nm, respectively. In contrast, the PNHOPC exhibited prominent amorphous structure, while only a little ordered arranged structure can be observed. The results indicate that the N-doping plays a major role in the etching effect. And the phosphorus in the carbon lattice can enhance the etching effect, which ultimately allows for more open edge sites and defect sites.

Raman spectra were collected to further characterize the carbon structure and degree of disorder. From Figure 2, it is clear that results from the Raman spectra are agree with the TEM results. The two conspicuous peaks near  $1345 \text{ cm}^{-1}$  and  $1590 \text{ cm}^{-1}$  are the D band and G band, respectively. For carbon-based materials, the intensity ratio of the D to G band ( $I_D/I_G$ ) is used to evaluate the degree of defects. Higher  $I_D/I_G$  values suggest more defects in the carbon structure. As shown in Figure 2, the  $I_D/I_G$  value of PNHOPC ( $\sim 0.95$ ) is higher than

that of PHOPC ( $\sim 0.86$ ) and NHOPC ( $\sim 0.92$ ). This result indicates that N-doping can significantly enhance the degree of defects in the carbon materials and that the additional incorporation of P can further enhance the disorder degree of the carbon materials.

The small-angle XRD patterns of the prepared catalysts are presented in Figure 3a. For all samples, a diffraction peak at  $2\theta = 0.5^\circ - 1.0^\circ$  was observed, which can be indexed to the  $(1\ 0\ 0)$  reflection of the hexagonal carbon structure. In particular, PHOPC shows a sharp and narrow diffraction peak at  $2\theta = 0.96^\circ$ , indicating that it possesses a well-ordered mesostructure. However, for NHOPC or PNHOPC, the peak at  $2\theta = 0.96^\circ$  is broader and less intense than that of PHOCH, suggesting that PHOCH has the highest ordered degree of the hexagonal mesostructure. Furthermore, the diffraction peak of PNHOPC is broader and less intense compared to that of NHOPC, indicating that PNHOPC has the lowest degree of order structure among the three samples.

Figure 3b presents the wide-angle XRD patterns of the three catalysts. Two diffraction peaks at  $24.3^\circ$  and  $43.5^\circ$  can be observed for PNHOPC, which are indexed to the  $(0\ 0\ 2)$  and  $(1\ 0\ 1)$  reflections of carbon,<sup>24, 25</sup> suggesting a low degree of graphitization. A sharp diffraction peak at  $26.5^\circ$  along with a resolved diffraction peak at  $43^\circ$  for PHOPC can also be observed, which can be indexed to the  $(0\ 0\ 2)$  and  $(1\ 0\ 1)$  reflections of typical graphite-like carbon<sup>26</sup> [powder diffraction

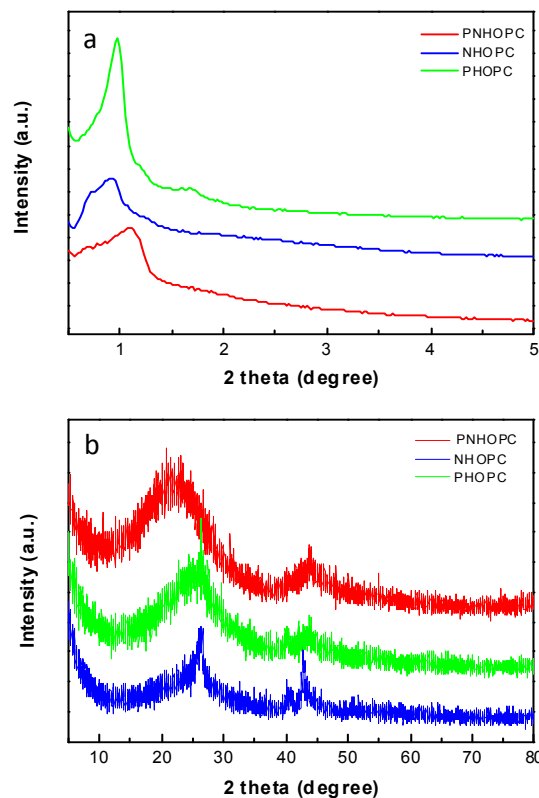


Figure 3. Small-angle (a) and wide-angle (b) X-ray diffraction (XRD) patterns.

file (PDF) number: 97–002–9123], and the NHOPC also shows discernible weak graphite peaks. The results indicate that N-doping has a stronger destructive effect and that the destruction of the graphite structure can be reinforced through co-doping N and P.

Figure 4 shows the  $N_2$  sorption isotherms and pore size distributions of the three samples, and Table S1 lists the corresponding textural parameters. Typical type IV isotherms with an  $H_1$ -type hysteresis loop (characteristic of mesoporous materials possessing an ordered hexagonal structure) were observed for all the samples. The inflections between the relative pressures  $P/P_0 = 0.4$ – $0.8$  in these isotherms correspond to capillary condensation within uniform mesopores. The narrow pore size distributions of PHOPC, NHOPC and PNHOPC are located at 3.4, 3.3 and 4.1 nm, respectively. Furthermore, large pore distributions ( $\sim 50$ – $110$  nm) of PNHOPC and NHOPC are also observed, which are likely attributed to the etching effect of N-doping by the  $NH_3$  treatment. As shown in Table S1, the BET surface areas are  $448\text{ m}^2\text{ g}^{-1}$ ,  $903\text{ m}^2\text{ g}^{-1}$  and  $1118\text{ m}^2\text{ g}^{-1}$ . The total pore volume varies from 0.38 to 0.74 and  $1.14\text{ cm}^3\text{ g}^{-1}$  for PHOPC, PNHOPC and NHOPC, respectively. This result demonstrates that the resulting PNHOPC possesses the highest

surface area and the largest pore volume with a dominant uniform pore size distribution.

The XPS analysis indicates that P and/or N are doped into the carbon at the surface (Table S2). The N concentration in NHOPC is 4.45% (atomic %), and it decreases to 3.32% with the additional doping of P. The Fe contents in NHOPC, PHOPC, and PNHOPC are 0.33%, 0.4% and 0.41% Fe-doping, respectively. The concentrations of phosphorous in PHOPC and PNHOPC are 0.22% and 0.16%, respectively. Figures 5a and 5b show the  $N1s$  XPS spectra of NHOPC and PNHOPC, which can be deconvoluted into five peaks assigned to pyridinic N (398.3 eV), Fe-N (399.1 eV), pyrrolic N (399.8 eV), graphitic N (400.9 eV) and pyridinic oxide (402.7 eV).<sup>7</sup> The concentrations of the different N groups are listed in Table S2. It can be observed that the concentrations of pyridinic N and graphitic N in NHOPC and PNHOPC are similar. However, the XPS spectrum of PNHOPC shows an intense Fe-N peak compared with that of NHOPC. Approximately 16 atomic % of the concentration of Fe-N sites at the carbon surface is increased after the additional P-doping (Table S2), which can contribute to high ORR activity. Moreover, the concentration of pyrrolic N is also increased after the additional P-doping.

The P in PHOPC and PNHOPC is analyzed, and the results are shown in Figures 5c and 5d. In PNHOPC, P is presented in the form of P-Fe, P-O and P-C,<sup>27, 28</sup> with P-O being the dominant phase. However, no obvious P-Fe peak was detected in PHOPC, which suggests that N-doping promotes the formation of P-Fe. Considering the increased amount of Fe and Fe-N sites after the additional P-doping, a synergistic effect exists between N, P and Fe, which contributes to the formation of Fe-N and Fe-P sites.

Furthermore, the  $C1s$  XPS spectra of the prepared catalysts are shown in Figure S1. For bare graphite, the binding energy of the C-C bond is 284.5 eV. However, the binding energy of NHOPC is up-shifted by 0.15 eV, which indicates that some of the electrons of the C atoms are transferred to the doped N atoms. It has been reported that charge delocalization provides oxygen adsorption sites in the form of side-on adsorption,<sup>5, 8</sup> and they provide active sites for the ORR. PHOPC shows a peak corresponding to a C-C bond at 284.59 eV, which is 0.09 eV higher than that of bare graphite. This result can be attributed to the dominant P-O phase in PHOPC (Figure 5c). The electronegativity of the O atom, which is also bonded with the C atom, is enhanced because of the electron-donating ability of P. As the oxygen bridge is formed between P and C, the O atoms with higher electronegativity ( $> 3.44$ ) can further enhance the charge delocalization of the C atom. Therefore, for PNHOPC, the peak corresponding to the C-C bond is up-shifted by 0.25 eV due to the charge delocalization caused by direct effect of N-doping and indirect effect of P-doping.

### 3.2 Electrocatalytic evaluations

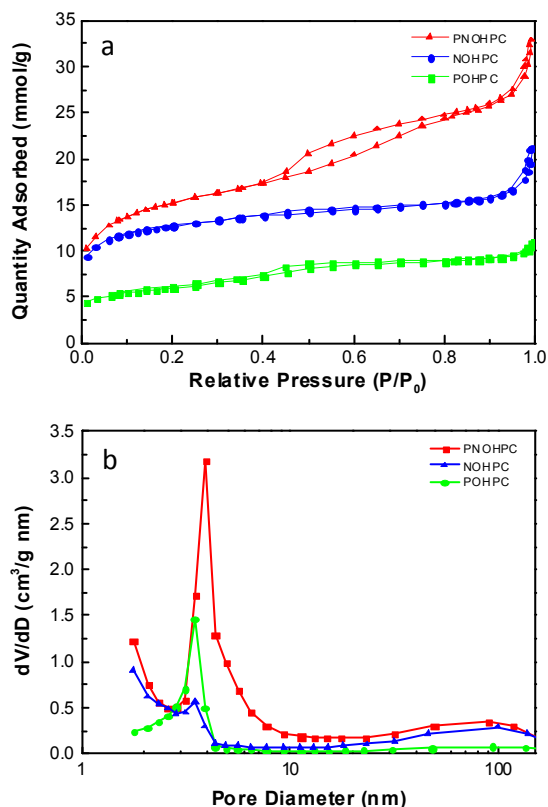


**Figure 4.**  $N_2$  sorption isotherms (a) and the corresponding pore size distribution curves (b) of NHOPC, PHOPC and PNHOPC.

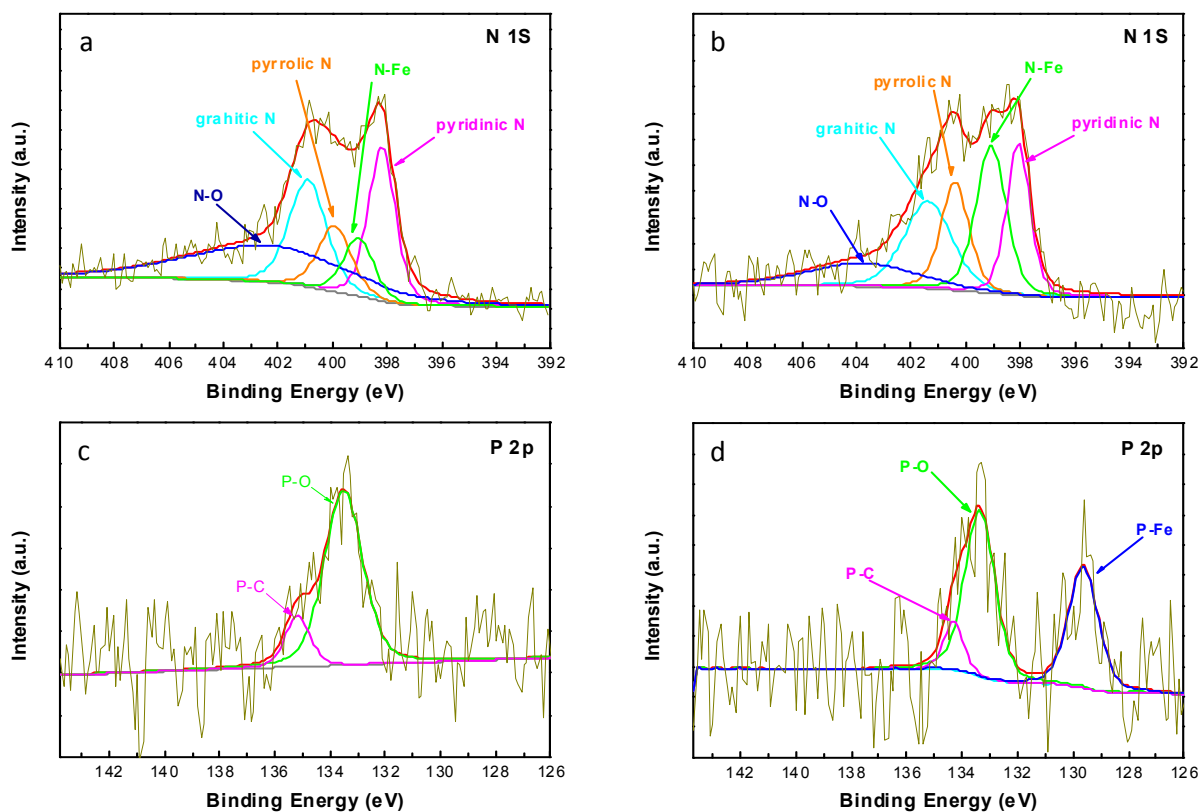


Figure 5. Analysis of the doping types for N in (a) NHOPC and (b) PNHOPC and of the doping type for P in (c) PHOPC and (d) PNHOPC

Linear sweep voltammetry (LSV) on a rotating disk electrode (RDE) was conducted to investigate the ORR activity. The polarization for the ORR on the catalysts is shown in Figure 6a. As a reference, a commercially available 20 wt. % Pt/C catalyst was measured. As shown in Figure 6a, the PNHOPC catalyst exhibits the best ORR catalytic activity with an onset potential of 0.89 V compared with the NHOPC (0.84 V) and the PHOPC (0.68 V) catalysts. Apparently, better performance for the ORR is obtained after the co-doping of N and P. For PNHOPC, high ORR activity is also inferred from the half-wave potential ( $E_{1/2}$  = 0.73 V), which is close to that of the Pt/C catalyst ( $E_{1/2}$  = 0.81

V). The ORR performances in acidic media for PNHOPC and other non-noble metal ORR electrocatalysts are compared by comparing the over potential of the ORR at three given low current densities ( $0.5 \text{ mA cm}^{-2}$ ,  $1 \text{ mA cm}^{-2}$ ,  $2 \text{ mA cm}^{-2}$ ). The results and the state of art of ORR electrocatalysts are shown in Table S3. Commercially obtained Pt/C (20 wt. %, JM Co.) was also examined under the same conditions for comparison. For the PNHOPC, the over potentials at the current density of  $0.5 \text{ mA cm}^{-2}$ ,  $1 \text{ mA cm}^{-2}$  and  $2 \text{ mA cm}^{-2}$  are 410 mV, 440 mV and 478 mV respectively, suggesting one of the most active catalysts toward the ORR. Additionally, the limiting diffusion

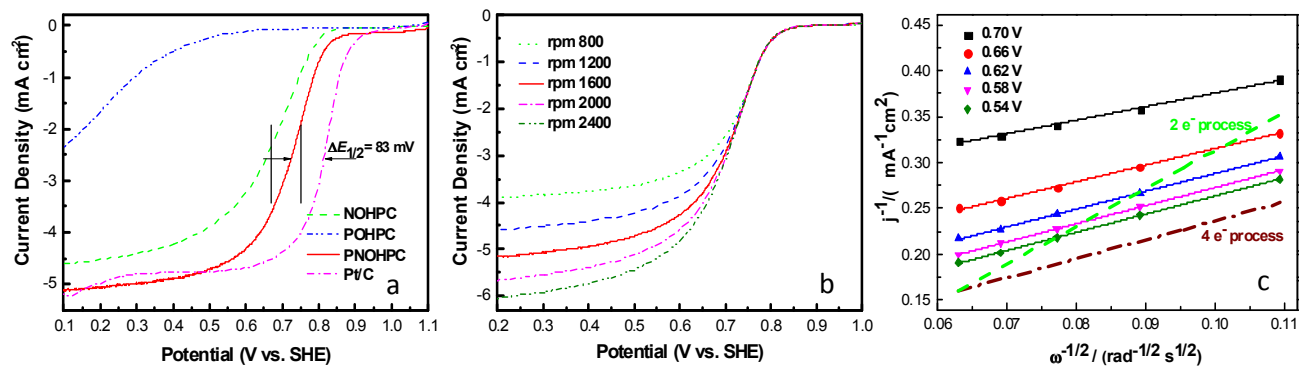
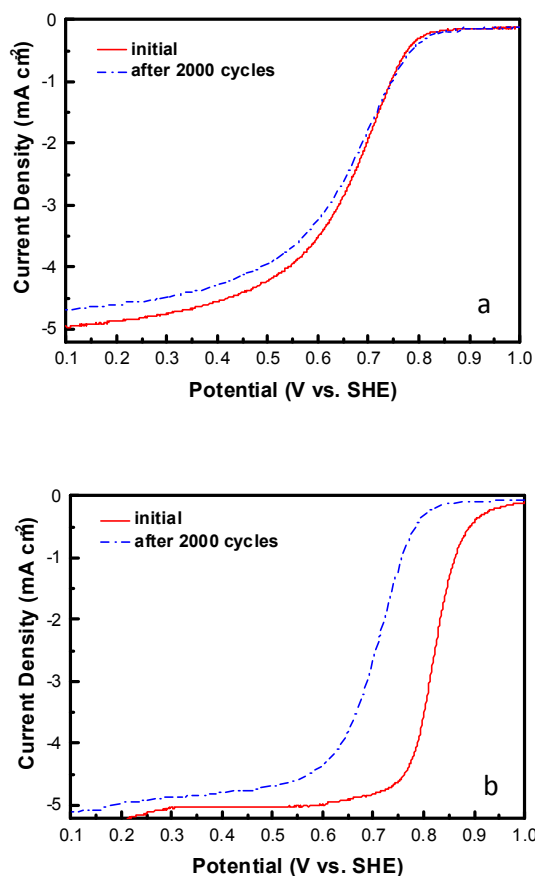
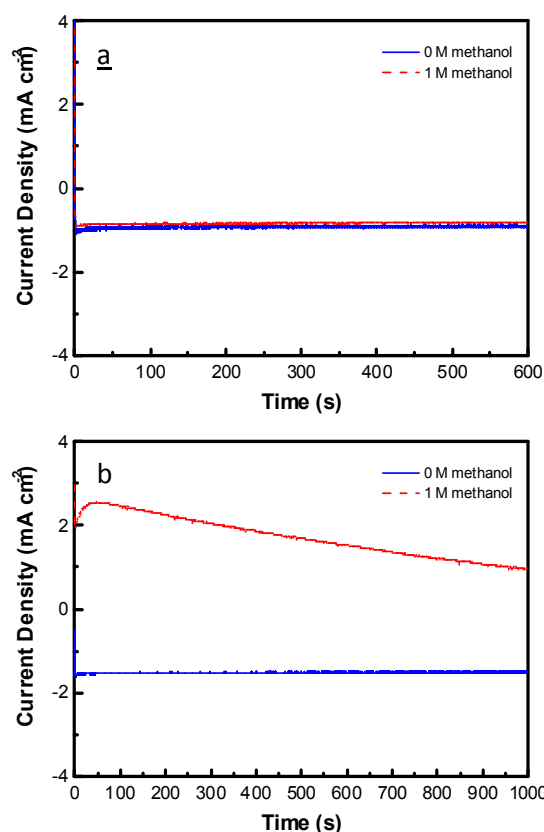


Figure 6. Electrocatalytic ORR in O<sub>2</sub>-saturated 0.5 M H<sub>2</sub>SO<sub>4</sub>: (a) ORR polarization curves for NHOPC, PHOPC, PNHOPC and Pt/C catalysts at a rotation rate of 1600 rpm; (b) ORR polarization curves for PNHOPC at a rotation rate from 800 to 2400 rpm; and (c) the corresponding Koutecky-Levich plots for PNHOPC at different potentials..

current of PNHOPC ( $5.13 \text{ mA cm}^{-2}$ ) is higher than that of the Pt/C catalyst ( $5.04 \text{ mA cm}^{-2}$ ). Then, comparing PHOPC and NHOPC, it is found that the N-doping has a much more significant influence on the ORR performance than the P-doping. Moreover, a positive shift of the half-wave potential and an increased limiting diffusion current are observed after the further addition of P, which could be due to the enhanced asymmetric spin density of carbon atoms and the effect on the structure. According to XPS results, for PNHOPC, phosphorus atoms with electron donate ability are mainly existed in the P-O phase, making the electronegativity of the O atom enhanced. Consequently, it promotes the charge delocalization of the C atoms, which is favorable for the adsorption of  $\text{O}_2$ . The formation of P-Fe and the increased amount of Fe and Fe-N sites after the additional P-doping, which suggests a synergistic effect between N, P and Fe, may also improve the catalytic performance. Moreover, the improved activity of PNHOPC can be attributed to high surface area and more open edge sites and defect sites. To further investigate the electrocatalytic mechanism and predominant process, a detailed study of a PNHOPC-modified



**Figure 7.** Accelerated durability test: ORR activities of (a) PNHOPC and (b) Pt/C in  $0.5 \text{ M H}_2\text{SO}_4$  before and after 2000 cycles of CV ( $-0.25$  to  $0.96 \text{ V vs. SCE}$  of CV range, and  $100 \text{ mV/s}$  scan rate).



**Figure 8.** Chronoamperometric responses for ORR with PNHOPC (a) and Pt/C (b) in  $\text{O}_2$ -saturated  $0.5 \text{ M H}_2\text{SO}_4$  with and without the addition of  $1 \text{ M CH}_3\text{OH}$ .

RDE at different rotating speeds was performed (as shown in Figure 6b). Based on the Koutecky-Levich (K-L) equation, the corresponding plots of  $j^{-1}$  versus  $\omega^{-1/2}$  at different potentials are shown in Figure 6c. The resulting K-L plots are linear, which suggests a first-order reaction toward the concentration of dissolved oxygen. As calculated from the slope of the plots, the electron transfer number of Pt/C for the ORR is 4.18 at  $0.62 \text{ V}$ , indicating that the ORR catalyzed by PNHOPC is dominated by an efficient four-electron ( $4 e^-$ ) process.

The durability of the PNHOPC catalyst was assessed using an accelerated durability test that cycles the catalysts between  $-0.25$  and  $0.96 \text{ V vs. SCE}$ . The ORR activities of PNHOPC and Pt/C after 2000 cycles and the negative shift of the half-wave potential were investigated (Figure 7). After 2000 continuous cycles, the half-wave potential  $E_{1/2}$  of PNHOPC exhibits a very small negative shift of  $\sim 14 \text{ mV}$ , suggesting its excellent durability (Figure 7a). As shown in Figure 7b, the Pt/C catalyst ( $90 \text{ mV}$  negative shifts after 2000 cycles) exhibits considerably lower durability. Moreover, the ORR activities of the PNHOPC and Pt/C catalysts are almost equal after 2000 cycles, making PNHOPC one of the most durable electrocatalysts for the ORR. It is also important to have an excellent catalytic selectivity for the cathode reaction against fuel oxidation, such as methanol oxidation. Therefore, the methanol tolerances of the PNHOPC

and Pt/C catalysts were evaluated in the presence of 1 M methanol. The PNHOPC catalyst shows little activity loss (Figure S2a), exhibiting excellent tolerance to methanol. In contrast, a considerably decreased ORR activity and a methanol oxidation reaction (MOR) peak are obtained for the Pt/C catalyst (Figure S2b). To further investigate the methanol tolerance, chronoamperometric measurements were performed at a constant voltage of 0.46 V (Figure 8). PNHOPC showed a stable ORR cathodic current. For the Pt/C catalyst, an anodic current of MOR was observed, indicating a low catalytic selectivity for the ORR. Furthermore, the stable ORR cathodic current of PNHOPC also demonstrates its remarkable durability.

## Conclusions

In summary, we have synthesized PNHOPC, NHOPC and PHOPC with hierarchically ordered porous structures via an evaporation-induced self-assembly process. Among the three materials, PNHOPC exhibits the best ORR catalytic performance, including the most positive onset potential (0.89 V) and the highest current density (5.13 mA cm<sup>-2</sup>). The over potential (@0.5 mA/cm<sup>2</sup>) of ORR catalyzed by the PNHOPC is reduced to 410 mV, which is one of the most active non-Pt ORR catalysts that have been reported. The phosphorus in the carbon lattice can induce more open edge sites and defect sites that enhance the degree of disorder in the carbon materials. Furthermore, the synergistic effect between N, P and Fe in PNHOPC and the enhanced charge delocalization via the P-O bond after the incorporation of phosphorus can improve the ORR catalytic performance. Moreover, PNHOPC shows high stability and excellent methanol tolerance. Additionally, the ORR process on the PNHOPC catalyst is proven to follow the four-electron transfer pathway. All of these features indicate that the PNHOPC catalyst is a highly promising non-precious metal ORR catalyst for the next generation of highly efficient metal-free ORR catalysts in fuel cells and metal-air batteries.

## Acknowledgements

The authors acknowledge financial support from the National Program on Key Basic Research Project (973 Program, 2012CB215500) and the authors acknowledge financial support from the Youth Innovation Promotion Association, CAS (No.2015147).

## Notes and references

1. Z. Yang, H. Nie, X. Chen, X. Chen and S. Huang, *J. Power Sources*, 2013, **236**, 238-249.
2. F. Jaouen, E. Proietti, M. Lefèvre, R. Chenitz, J.-P. Dodelet, G. Wu, H. T. Chung, C. M. Johnston and P. Zelenay, *Energ. Environ. Sci.*, 2011, **4**, 114-130.
3. R. Othman, A. L. Dicks and Z. Zhu, *Int. J. Hydrogen Energ.*, 2012, **37**, 357-372.

4. A. Morozan, B. Josselme and S. Palacin, *Energ. Environ. Sci.*, 2011, **4**, 1238.
5. Y. Zhao, L. Yang, S. Chen, X. Wang, Y. Ma, Q. Wu, Y. Jiang, W. Qian and Z. Hu, *J. Am. Chem. Soc.*, 2013, **135**, 1201-1204.
6. X. Zhao, Q. Zhang, B. Zhang, C.-M. Chen, A. Wang, T. Zhang and D. S. Su, *J. Mater. Chem.*, 2012, **22**, 4963-4969.
7. H. Peng, Z. Mo, S. Liao, H. Liang, L. Yang, F. Luo, H. Song, Y. Zhong and B. Zhang, *Sci. Rep.*, 2013, **3**, 1765.
8. Y. Liu, S. Chen, X. Quan, H. Yu, H. Zhao, Y. Zhang and G. Chen, *J. Phys. Chem. C*, 2013, **117**, 14992-14998.
9. Z. W. Liu, F. Peng, H. J. Wang, H. Yu, W. X. Zheng and J. Yang, *Angewandte Chemie*, 2011, **123**, 3315-3319.
10. D.-W. Wang and D. Su, *Energ. Environ. Sci.*, 2014, **7**, 576-591.
11. D.-S. Yang, D. Bhattacharjya, S. Inamdar, J. Park and J.-S. Yu, *J. Am. Chem. Soc.*, 2012, **134**, 16127-16130.
12. D. Nguyen-Thanh, A. I. Frenkel, J. Wang, S. O'Brien and D. L. Akins, *Appl. Catal., B*, 2011, **105**, 50-60.
13. E. Proietti, F. Jaouen, M. Lefèvre, N. Larouche, J. Tian, J. Herranz and J.-P. Dodelet, *Nat. Commun.*, 2011, **2**, 416.
14. J. Xi, Y. Xia, Y. Xu, J. Xiao and S. Wang, *Chemical communications*, 2015, **51**, 10479-10482.
15. A. H. A. Monteverde Videla, L. Zhang, J. Kim, J. Zeng, C. Francia, J. Zhang and S. Specchia, *Journal of Applied Electrochemistry*, 2012, **43**, 159-169.
16. H. Peng, Z. Mo, S. Liao, H. Liang, L. Yang, F. Luo, H. Song, Y. Zhong and B. Zhang, *Scientific Reports*, 2013, **3**.
17. C. W. B. Bezerra, L. Zhang, K. Lee, H. Liu, A. L. B. Marques, E. P. Marques, H. Wang and J. Zhang, *Electrochimica Acta*, 2008, **53**, 4937-4951.
18. K. Kwon, Y. J. Sa, J. Y. Cheon and S. H. Joo, *Langmuir*, 2011, **28**, 991-996.
19. A. H. M. Videla, L. Zhang, J. Kim, J. Zeng, C. Francia, J. Zhang and S. Specchia, *J. Appl. Electrochem.*, 2013, **43**, 159-169.
20. J. Xu and T. Zhao, *RSC Adv.*, 2013, **3**, 16-24.
21. C. Deng, H. Zhong, L. Yao, S. Liu, Z. Xu and H. Zhang, *ChemSusChem*, 2014, **7**, 3435-3441.
22. R. Bashyam and P. Zelenay, *Nature*, 2006, **443**, 63-66.
23. Y. Meng, D. Gu, F. Zhang, Y. Shi, L. Cheng, D. Feng, Z. Wu, Z. Chen, Y. Wan and A. Stein, *Chem. Mat.*, 2006, **18**, 4447-4464.
24. H. Zhong, H. Zhang, S. Liu, C. Deng and M. Wang, *ChemSusChem*, 2013, **6**, 807-812.
25. S. Liu, H. Zhang, Z. Xu, H. Zhong and H. Jin, *International Journal of Hydrogen Energy*, 2012, **37**, 19065-19072.
26. S. Liu, H. Zhang, Z. Xu, H. Zhong and H. Jin, *Int. J. Hydrogen Energ.*, 2012, **37**, 19065-19072.
27. Y. Cao, H. Yu, J. Tan, F. Peng, H. Wang, J. Li, W. Zheng and N.-B. Wong, *Carbon*, 2013, **57**, 433-442.
28. U. B. Nasini, V. Gopal Bairi, S. Kumar Ramasahayam, S. E. Bourdo, T. Viswanathan and A. U. Shaikh, *ChemElectroChem*, 2014, **1**, 573-579.